Developmental Biology 461 (2020) 184–196

Contents lists available at ScienceDirect

Developmental Biology

journal homepage: www.elsevier.com/locate/developmentalbiology

Original research article

Visualizing mesoderm and neural crest cell dynamics during chick head morphogenesis

Mary Cathleen McKinney [a], Rebecca McLennan [a], Rasa Giniunaite [b], Ruth E. Baker [b], Philip K. Maini [b], Hans G. Othmer [c], Paul M. Kulesa [a,d,*]

[a] Stowers Institute for Medical Research, Kansas City, MO, 64110, USA
[b] University of Oxford, Wolfson Centre for Mathematical Biology, Mathematical Institute, Woodstock Road, Oxford, OX2 6GG, UK
[c] School of Mathematics, 270A Vincent Hall, University of Minnesota, Minneapolis, MN, 55455, USA
[d] Department of Anatomy and Cell Biology, University of Kansas School of Medicine, Kansas City, KS, 66160, USA

ARTICLE INFO

Keywords:
Time-lapse
Tissue growth
Neural crest
Mesoderm
Avian
Computer modeling

ABSTRACT

Vertebrate head morphogenesis involves carefully-orchestrated tissue growth and cell movements of the mesoderm and neural crest to form the distinct craniofacial pattern. To better understand structural birth defects, it is important that we characterize the dynamics of these processes and learn how they rely on each other. Here we examine this question during chick head morphogenesis using time-lapse imaging, computational modeling, and experiments. We find that head mesodermal cells in culture move in random directions as individuals and move faster in the presence of neural crest cells. In vivo, mesodermal cells migrate in a directed manner and maintain neighbor relationships; neural crest cells travel through the mesoderm at a faster speed. The mesoderm grows with a non-uniform spatio-temporal profile determined by BrdU labeling during the period of faster and more-directed neural crest collective migration through this domain. We use computer simulations to probe the robustness of neural crest stream formation by varying the spatio-temporal growth profile of the mesoderm. We follow this with experimental manipulations that either stop mesoderm growth or prevent neural crest migration and observe changes in the non-manipulated cell population, implying a dynamic feedback between tissue growth and neural crest cell signaling to confer robustness to the system. Overall, we present a novel descriptive analysis of mesoderm and neural crest cell dynamics that reveals the coordination and co-dependence of these two cell populations during head morphogenesis.

1. Introduction

Vertebrate head morphogenesis is a process that involves the rapid growth and dynamic behaviors of several cell populations to form the face, jaw, and branchial arches. These cell populations, that include the ectoderm, mesoderm and neural crest, must be coordinated in a well-orchestrated choreography to produce the proper axial pattern of the head. For example, to reach the periphery after exiting the dorsal neural tube, cranial neural crest cells must travel through dense extracellular matrix and mesoderm, subjacent to the ectoderm (Tosney, 1982; Noden, 1988). Tissue transplantations, together with viral and fluorescent dye marking of the cranial neural crest and paraxial mesoderm, have revealed that both cell types are migratory and follow stereotypical pathways into the branchial arches (Kontges and Lumsden, 1996; Hacker and Guthrie, 1998; Evans and Noden, 2006). However, these static analyses have not been able to tease out the cell dynamics and the relationship between cell proliferation, tissue growth and cell-cell interactions that contribute to the complexity of head morphogenesis. This is primarily due to the lack of a detailed *in vivo* analysis of head mesoderm and ectoderm dynamics in space and time, and limitations with *in vivo* imaging of neural crest-mesodermal cell interactions.

A better understanding of the dynamics and interplay between the neural crest and tissues through which these cells travel would shed light on the mechanistic basis of collective cell migration, for which neural crest cells are an exemplary model (reviewed in Noden and Trainor, 2005; Kulesa and McLennan, 2015; Szabo and Mayor, 2016). Detailed experiments, together with mathematical modeling, provide a means to explore the robustness of the stereotypical cranial neural crest cell migratory pathways and distance migrated by cells during early head development under the constraints of a growing

* Corresponding author. Stowers Institute for Medical Research, Kansas City, MO, 64110. USA.
E-mail address: pmk@stowers.org (P.M. Kulesa).

https://doi.org/10.1016/j.ydbio.2020.02.010
Received 20 December 2019; Received in revised form 12 February 2020; Accepted 14 February 2020
Available online 19 February 2020

microenvironment. In the absence of dynamic data, it is possible to speculate on a wide variety of tissue growth profiles for the head mesoderm and their potential impact on collective neural crest cell migration. For example, in previous work, we quantified a curvilinear measurement of the distance from the chick neural tube dorsal midline along the dorsolateral cranial neural crest cell migratory pathway, to the tip of branchial arch 2 (ba2) throughout early developmental stages (McLennan et al., 2012, 2017). This simple length measurement revealed a logistic growth profile of the total neural crest cell migratory domain over time (McLennan et al., 2017), but left unanswered the question of whether there is non-uniform growth of the mesoderm in space.

In this study, we investigate the spatial and temporal dynamics of individual mesoderm and ectoderm cells, and their interplay with migrating neural crest cells during head morphogenesis. We examine and quantify the inherent migratory properties of mesoderm either isolated from, or in the presence of, neural crest cells, as a baseline for *in vivo* comparison. We then visualize and quantify head ectoderm, mesoderm and neural crest cell behaviors simultaneously in Tg(hUBC:H2BCerulean-2A-Dendra2) whole quail embryo explants. We image BrdU and methyl green nuclear labels in cleared whole chick embryos to distinguish proliferative subregions within the head mesoderm throughout successive chick developmental stages during neural crest cell migration. In addition, we computationally explore the impact of different spatially non-uniform mesoderm growth profiles and converge on a subset of possible outcomes that result in a continuous neural crest cell migratory stream. To address how changes in either the presence of neural crest cells or mesodermal cell proliferation affect cell dynamics and branchial arch size, we ablate a subregion of premigratory neural crest cells and measure subsequent tissue growth. Separately, we apply aphidicolin and hydroxyurea by focal microinjection into paraxial mesoderm to inhibit cell proliferation and compare the distribution of neural crest cells along the migratory domain with our computational model predictions. Together, our data offer the first detailed characterization of cell and tissue growth dynamics in the vertebrate head, and how neural crest cells must respond to migrate in a collective and directed manner.

2. Materials and methods

2.1. Embryos and in ovo labeling

Fertilized white leghorn chicken (Centurion Poultry) or Tg(hUBC:H2BCerulean-2A-Dendra2) quail eggs (Translational Imaging Center, University of Southern California) were incubated at 38 °C in a humidified incubator until the desired Hamburger and Hamilton (HH) stage (Hamburger and Hamilton, 1951) of development. A 0.3M sucrose solution was mixed 1:1 with DiD vibrant dye solution (V22887 Thermo Fisher) and injected into the neural tubes of embryos at HH9 for neural crest labeling.

2.2. In vitro assays

For mesoderm and neural tube cultures, glass bottomed petri dishes (P35G-1.5–20C, Mattek) were coated with 20ug/ml of fibronectin (F1141; Millipore Sigma) and 20ug/ml of poly-D-lysine (P7886; Millipore Sigma) for 30 minutes (mins) before being allowed to dry. Lateral mesoderm tissue from the r4 axial level was isolated from stage HH6-8 chick embryos by creating transverse cuts at the r3/r4 and r4/r5 borders and then removing neural tube, ectoderm and endoderm with a sharpened tungsten needle and forceps. The remaining mesoderm was placed onto prepared glass bottomed dishes. Isolated neural tube explants were prepared as previously described (McLennan et al., 2010) and placed in a separate dish or near the mesoderm tissue. Cells were cultured in Ham's F-12 nutrient mix (11765047; Thermo Fisher) supplemented with Pen/Strep and B27 (17504044, Thermo Fisher) at 37° either in a tissue culture incubator or in an environmental chamber on the microscope. For *in vitro* experiments with VEGF, 100ug/mL of VEGF (293-VE-010, R&D systems) was added to the F-12 media for 16 hours (hrs) incubation or PBS for control. Cells were labeled with 5ug/mL of Hoechst 33342 (b2261, Millipore Sigma) for 10 mins either for live imaging or after immunohistochemistry. Glass bottomed dishes for *in vitro* cultures were placed in a 6-well microscope stage insert inside a heated environmental chamber on an LSM-800 confocal microscope (Zeiss) and imaged in 5 min intervals, using a Plan Apochromat 10 × 0.45 NA M27 objective, single z plane, with a minimum of 405 laser intensity for 16 or more hours. Analysis was performed on many cells from multiple time lapses (three mesoderm/neural tube, five mesoderm only, four neural tube only, three mesoderm and ectoderm). Significance was determined with a two-tailed Student's T-test throughout the manuscript.

2.3. Antibody labeling

For proliferation studies *in vivo*, the vitelline membrane was removed from the head of the embryo and then 50uL of BrdU labeling reagent (000103, Thermo Fisher) was dropped on top. The embryos were reincubated for 30 mins then fixed in 4% paraformaldehyde overnight at 4°. The head and first four somites were isolated from the trunk and then embryos HH13 and older were bisected down the midline. For immunohistochemistry, fixed embryos were incubated for 10 mins in 1N HCl on ice, 10 mins in 2N HCl at room temperature followed by 20 mins at 37°. After 12 mins in Borate buffer, the embryos were incubated with PBS+1% TritonX and finally 10% goat serum (16210072, Thermo Fisher) block. *In vitro* cultures were prepared by adding 1% BrdU labeling reagent and cultured for 1 hr before fixing with 4% paraformaldehyde for 30 mins at room temperature. *In vitro* protocols only require 15 mins 1N HCl at 37° and 15′ Borate buffer before washing and blocking. Embryos or cells were labeled with primary antibodies BrdU (1:200, pa5-32256, ThermoFisher, Lot TH2627941A) and HNK-1 (1:25, TIB-200, ATCC) in block overnight at 4°. After extensive washing in block at room temperature, secondary antibodies-goat anti-rabbit IgG Alexa Fluor 488 and goat anti-mouse IgM AlexaFluor 546 (A-11008 and A-21045, Thermo Fisher) were applied at a 1:500 dilution overnight at 4°. For a nuclear stain, Methyl Green (1:5000, M8884 Millipore Sigma (Prieto et al., 2015)) was added to embryos after immunohistochemistry for several hours. Embryos with no primary antibody were used as control. Embryos were cleared for imaging using 80% FRUIT clearing buffer (Hou et al., 2015) overnight at 4° and mounted for imaging in 80% FRUIT buffer on glass slides. At least 3, and up to 5, embryos' data were combined for each stage.

2.4. Embryo manipulations

Bilateral ablations of the dorsal 1/3 of the neural tube were performed on HH9 embryos *in ovo*. Using a glass needle and forceps, a cut was created down the midline from r3 to r5 and the dorsal aspect neural tube was removed. Control embryos were opened, staged and re-sealed. After 24 hr incubation, embryos were treated with BrdU reagent as above for 30 mins then harvested and processed for immunohistochemistry. To halt proliferation in the mesoderm, Stage HH10 embryos *in ovo* were injected with a freshly prepared cocktail of 100ug/mL Aphidicolin (A0781, Millipore Sigma), 5mM hydroxyurea (H8627 Millipore Sigma), and 10% DiD. Injections were made at the axial level of r3 to r5 as lateral as could be reached but still in the mesoderm. DiD was used to visualize the area injected and give a rough estimate of where the chemicals were distributed. Control embryos were injected with 10% DMSO and DiD. After injection, embryos were resealed and incubated for 8 hrs then fixed and processed for immunohistochemistry. Thirteen injected and eight control embryos were used for analysis.

2.5. Microscopy

Live embryos for time lapse imaging were mounted on EC culture dorsal-side down beginning at HH9 or 10 as previously described (Chapman et al., 2001; McKinney et al., 2016) such that the EC culture was plated with only 500uL of liquid to reduce light scattering. Confocal z-stacks using 488nm laser to image Dendra2 of the transgenic quail and 633 for DiD were collected every 7 min for up to 12 hrs with a 10x 0.45 objective. Embryos used for photoconversion were mounted similarly on EC culture. Regions approximately 100x100 μm for Dendra2 photoconversion were chosen on both sides of the embryo if possible. 5% 405nm laser was scanned in this region and fluorescence intensity of Green Dendra and Red Dendra were monitored in a second channel until the Red intensity no longer increased. A larger, tiled z-stack image of the whole head was then acquired. Embryos were transferred to an incubator for 6–8 hrs then removed from the culture dish by a paper ring, mounted on a glass slide and immediately re-imaged in a tiled z-stack. Fixed embryos were imaged in 80% FRUIT clearing buffer in tiled, z-stack images with a Plan Apochromat 10 × 0.45 NA objective on an LSM-800 microscope. Microscopy was optimized for imaging AlexaFluor 488, AlexaFluor 546 and methyl green.

2.6. Image analysis

Both *in vitro* and *in vivo* time-lapse imaging series were concatenated and aligned (Preibisch et al., 2010) in Fiji (Schindelin et al., 2012). *In vivo* time-lapses were aligned so that the most dorsal cells at the midline at the center of rhombomere 4 were centered throughout the time-lapses. In this way, multiple movies can be overlaid keeping the spatial information comparable between embryos. Post alignment, images were imported into Imaris (Bitplane AG) for tracking cells with fluorescent labels. *In vitro* mesodermal cells and neural crest cells were tracked by hand due to the single color labeling of the nuclei. If a cell moved into a very dense area or a track could become confused with another cell, the track was stopped. Embryonic cells were tracked semi-automatically with Imaris. Track position and statistics were exported to MATLAB (Mathworks Inc) scripts for further analysis. Distance between random cells (Fig. 2D,F) was calculated only for the time both cells existed. If a division occurred, then one random daughter was picked. Images of BrdU, methyl green and HNK1 labeled embryos were first stitched in Fiji (Preibisch et al., 2009), then imported to Imaris for segmentation. Images were smoothed, attenuation corrected and then the domain around the r4 neural crest stream was isolated by hand. For younger embryos with little or no neural crest present, an area was selected dorsal to the neural tube at the r4 axial level across to the lateral end of the tissue directly across from r4. The width was chosen based on shape of the neural tube. For older embryos, the region of interest was selected from around the neural crest stream down to the most lateral end of the tissue. Similar procedures were followed for the stream of neural crest targeting ba1. The area lateral to r3 was isolated by creating a 100 μm circle from the ectoderm between the ba1 and ba2 streams (including the ectoderm). Segmentation was performed on the methyl green signal. Separation of the ectoderm was achieved using a distance transformation to the original domain region and some hand-editing. While the HNK-1 signal is a membrane label, the channel is bright enough to create an intensity cut-off for neural crest identification at the nucleus. The bright BrdU signal allowed us to create an intensity cut-off for proliferation at the inflection point in a frequency histogram of all BrdU intensities. The average intensity, position and minimum distance to a neighbor were exported to MATLAB scripts for calculating the fraction of cells proliferating and average minimum distance to a neighbor in 50 μm bins down the length of the domain. For density measurements, a very rough surface was created in Imaris using the nuclei of cells so that the volume extended to the edge of the tissue. The surface was then cut along the migratory stream at 50um segments. The number of cells located in each segment and the surface volume were used to calculate density. MATLAB scripts can be obtained through Stowers Original Data Repository upon publication.

2.7. Computer model simulations

In the developing model, we assume that there are two types of cells, namely "leaders" and "followers". There are a fixed number of leaders who undertake a biased random walk with volume exclusion up a cell-induced gradient of chemoattractant. The leaders perform this biased random walk by extending three filopodia in random directions per time step. These filopodia are assumed able to sense the concentration of chemoattractant at their tip and the cell moves in the direction of the highest concentration sensed, provided it is higher than that at the position of the center of the cell. If this is not the case, then the cell moves in a random direction. On the other hand, followers are either in a chain or move randomly. A chain consists of a group of followers that are close to each other and at least one of the cells is close to a leader. All the followers in a chain move in the same direction as the leader that is at the front of the chain. If a follower is relatively close to more than one leader so that it may join more than one chain, then the cell randomly chooses which one to follow. We include a simplified version of phenotype switching between leaders and followers based on the position of a cell within a migratory stream (see Supplementary Methods).

We use experimental data to parameterize the initial and final lengths of the domain in the model and we carry out three studies. Initially, we consider uniform (U) domain growth throughout the domain. Then we split the domain into two parts, which we call proximal and distal subregions (Fig. 6A), that have different growth rates. We consider first making the difference in growth rates a factor of two (Fig. 6A; Distal (D) and Proximal (P)), and then a combination of distal and proximal growth (Fig. 6A; Mixed (M)). We assume exponential growth of the domain in time and pick the growth rates in such a way that each of the growth profiles leads to the same total domain length after 24 hrs. We run twenty simulations for each case and store statistics after 24 hrs on the density of cells along the domain, the furthest distance traveled (which we quantify as the average maximum distance traveled by the leader cells), and the fraction of the simulations with more than 20% follower cells not in chains (a measure of the likelihood of stream breakage).

3. Results

3.1. Head mesoderm and neural crest cells in culture are both inherently dynamic, but the cell behaviors are influenced by co-culture with each other

The growth of the vertebrate head is substantial during early development, with proliferation and migration of both mesodermal cells and neural crest cells (Fig. 1A). To better understand the inherent migratory properties of individual cranial paraxial mesodermal cells, we visualized and quantified cell trajectories of Hoechst-labeled mesoderm isolated from the embryo lateral to rhombomere 4 (r4) at HH6-8 (Hamburger and Hamilton, 1951) (Fig. 1B). Cultured mesodermal cells moved rapidly to disperse throughout the culture dish with an average cell speed of approximately 64 μm/hr and directionality (defined as distance from start to finish divided by the total distance traveled) of 0.22 (Fig. 1C and D). Mesodermal cell behaviors in culture resembled migrating neural crest cells with long, extended cellular processes that stretched between neighboring cells and open spaces of the culture dish (compare Movies 1, 2). Occasionally, we observed a few neural crest cells in the mesoderm explant (identified by HNK-1), but typically these cells were absent (Fig. S1).

Supplementary videos related to this article can be found at https://doi.org/10.1016/j.ydbio.2020.02.010.

In comparison, cranial neural crest cells that exited from explanted neural tubes moved with an average speed of 79 μm/hr and directionality of 0.19. Neural crest cells were statistically faster and cell trajectories were more circuitous than the mesoderm. We also visually observed that

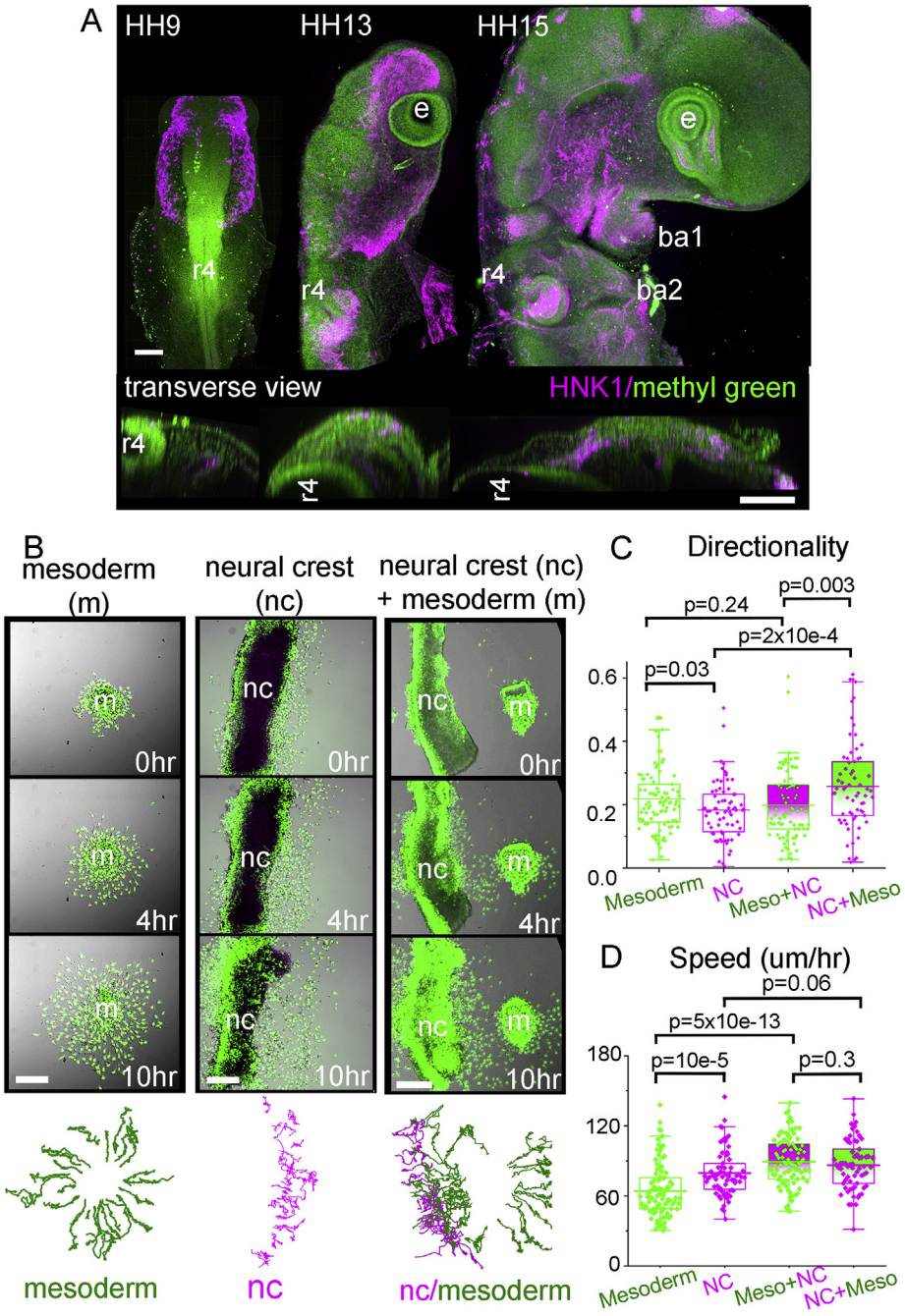

Fig. 1. Growing chick embryo and mesodermal cell migration. (A) Similarly scaled chick embryos between stages HH9 and HH15 showing the growth of the head. All nuclei (green) and neural crest (magenta) illustrate the increase in number of cells and size of the embryo over time. Upper images: lateral view, scale bar 150um. Lower images: transverse view at the level of r4, scale bar 50um. (B) Column 1: Mesodermal cells isolated from HH6-8 embryos grown *in vitro*. Final panel are tracks of individual cells over 10 hrs. Column 2: Neural tube from HH11 embryo cultured *in vitro*. Final panel tracks of neural crest cells. Column 3: Neural tube from HH11 embryo co-cultured with mesoderm sample. Final panel are tracks of neural crest cells (magenta) and mesoderm (green). Scale bars 50um. (C) Directionality and (D) Speed of mesoderm only (green, n = 5, 94 cells total), neural crest cells only (magenta, n = 4, 73 cells), mesodermal cells in the presence of neural crest (green markers with magenta box, n = 3, 91 cells) and neural crest in the presence of mesoderm (magenta markers with green box, n = 3, 66 cells).

cell exploratory behaviors and interaction of neighbors were similar. However, when we cultured mesoderm and neural tube explants together (Movie 3), both cell types increased their speed to 89 and 86 μm/hr, respectively. Only the mesodermal cell speed increased significantly (64–89 μm/hr; p = 5x10e-13) such that there was relatively no difference in speed between neural crest and mesodermal cells (Fig. 1D). On the other hand, neural crest cells were more directed in the presence of the mesoderm (Fig. 1C). Individual neural crest and mesodermal cells mixed freely, and some neural crest cells infiltrated the explanted intact mesoderm (Movies 3, 4). When we maintained the ectoderm with the intact mesoderm, we found the that mesoderm frequently adhered to the sheet of ectoderm and traveled with this tissue (Movie 5). Thus, chick head mesoderm is capable of dissociating and migrating as individual cells. These cells explored the culture dish in a similar manner to neural crest cells but moved faster when neural crest cells were present; neural crest cells responded to the mesoderm by becoming more directed.

Supplementary videos related to this article can be found at https://doi.org/10.1016/j.ydbio.2020.02.010.

3.2. *In vivo time-lapse imaging reveals distinct collective motions of head mesoderm and neural crest cell behaviors*

Time-lapse imaging and analysis was performed on the developing head of Tg(hUBC:H2BCerulean-2A-Dendra2) quail embryos (Huss and Lansford, 2017) with premigratory neural crest co-labeled with DiD (Fig. 2A). The neural crest, as well as neighboring mesoderm and ectoderm cell movements, were tracked during neural crest migration (Fig. 2A). Time-lapse movies were aligned so that the dorsal-most cells at the midline in the center of r4 were fixed in position. In this way, multiple movies can be compared while keeping the rough spatial location in the

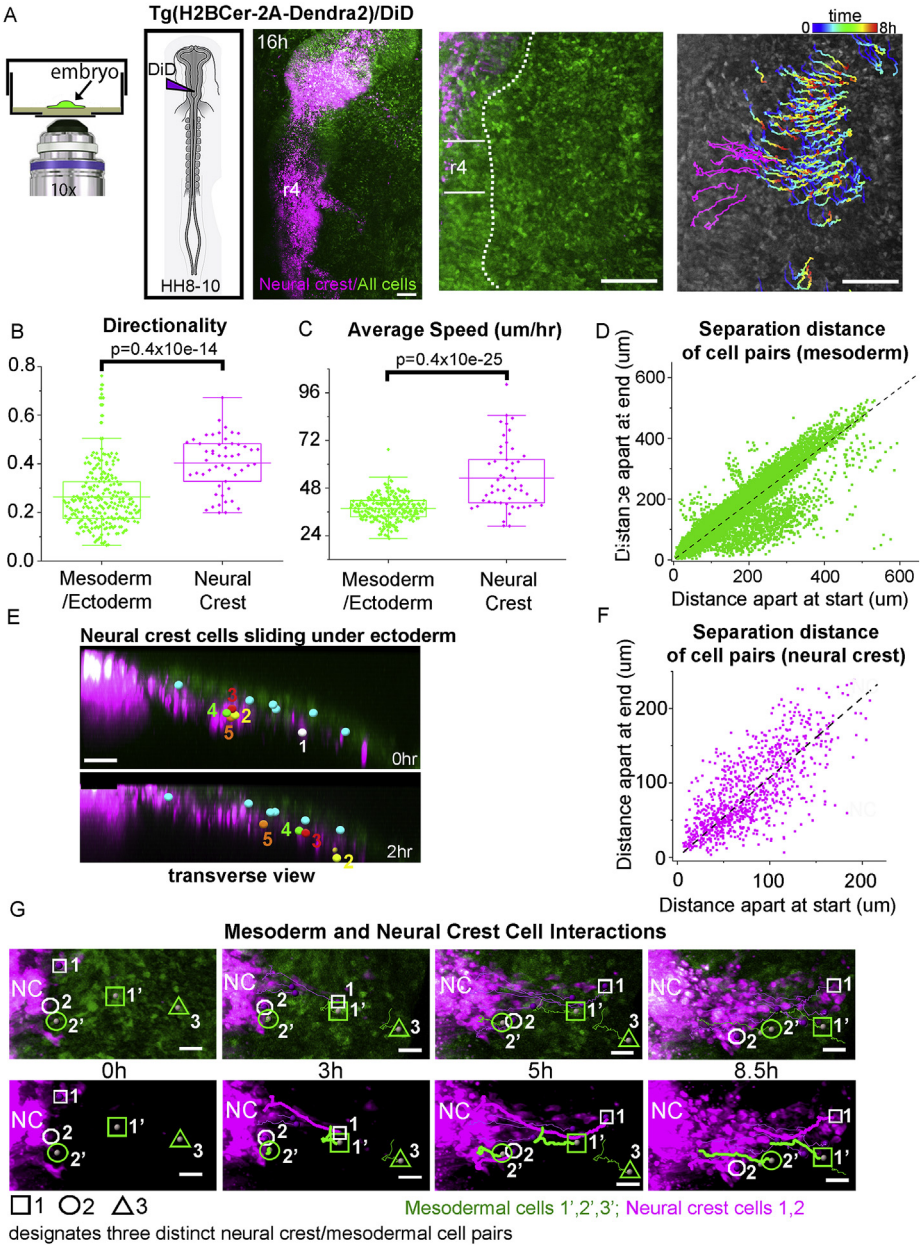

Fig. 2. Neural crest cells are faster and more directed than the surrounding mesoderm *in vivo*. (A) Schematic of a typical embryo mounted with EC culture media. Images of Dendra2 (green) transgenic quail roughly HH13 or 9 h into a time-lapse session with DiD labeling of premigratory neural crest (magenta). First image of example time-lapse with r4 and edge of neural tube marked. First image overlayed with tracks of mesoderm/ectoderm cells colored by time and neural crest cells in magenta. Scale bars 100um. Directionality (B) and Speed (C) of neural crest, mesoderm and ectodermal cells. n = 3 embryos each, 242 mesoderm/ectoderm cells and 74 neural crest cells. (D) Comparison of the separation distance between any two mesodermal cell pairs at the time of their first co-existence to their last observation, including pairs from different time-lapse movies. Straight line fit to data (dashed black). (E) Transverse view of r4 at HH12. Individual ectoderm cells (cyan), neural crest cells (numbered) showing the relative speed of neural crest compared to the neighboring tissue over a 2-h window. Scale bar 20um. (F) Separation distance for neural crest only. (G) Series of images from a typical time-lapse movie showing interaction between neural crest (magenta) and mesodermal cells (green) over 8.5 hrs. Circles (neural crest). Squares and Triangle (mesodermal cells). Scale bar 20um.

embryo. After the onset of neural crest emigration from r4 in the embryo (approximately HH11), we observed a generally lateral movement of mesoderm and ectoderm cells (Fig. 2A,D,F, Movies 6, 7). After neural crest cells invaded the mesoderm, mesodermal cells migrated with significantly higher directionality of 0.33 than *in vitro* (0.22), but moved more slowly at approximately 43 μm/hr (Fig. 2B,E). *In vivo*, the neural crest cells moved through the mesoderm significantly faster than the mesodermal cells (53 μm/hr) and with a significantly higher directionality of 0.40 (Fig. 2B,E). By the time that the neural crest cell migratory stream is fully defined adjacent to r4 (HH12), neural crest cells moved at an even faster speed (97.7 μm/hr, Fig. 2C, Movie 8). In contrast, individual ectoderm cells that directly overlie the dorso-lateral neural crest cell migratory pathway move slowly and are passed by the invading neural crest cells (Movie 8). We sought to find a pattern in the speed or directionality of the cells with respect to location in the embryo and found that the cells near r3 were the slowest tracked, but there was not a clear spatial pattern to speed or directionality (Fig. S2).

Supplementary videos related to this article can be found at https://doi.org/10.1016/j.ydbio.2020.02.010.

To quantify the rearrangement of cells during migration, we examined the distance between random pairs of cells at the beginning of the time-lapse to the same cells at the end of the time-lapse session (Fig. 2D). Mesodermal cells were observed to move as a uniform collection of cells; trailing cells did not overtake or leapfrog the leaders and maintained neighbor relationships (Fig. 2D). Mesodermal cells that were far apart, remained far apart as seen with cell pairs distributed along a straight line with slope approximately equal to 1 (Fig. 2D). Similar conclusions can be made of the neural crest which have been shown before to move as a uniform collection of cells without wholesale rearrangement (Fig 2F (Kulesa et al., 2008)).

Analysis of individual neural crest and mesodermal cell interactions revealed that mesoderm behaviors varied in at least three distinct ways (Fig. 2G, Movie 6). For example, a typical mesodermal cell positioned distal to the neural crest cell invasive front is eventually passed by rapidly moving neural crest cells (Fig. 2G, squares). For 2 h, this particular mesodermal cell maintained a straight trajectory parallel to the passing neural crest cells, then changed direction to move posterior near the entrance to the branchial arch. Second, as migrating neural crest cells

collided with mesodermal cells, the mesodermal cells were observed to match the neural crest stream direction and move along with the stream as though the cells were pushed (Fig. 2G, circle). Third, some mesodermal cells located very distal to the emerging neural crest cell migratory stream moved slowly enough that neural crest cells leapfrogged to move further distally (Fig. 2G, triangle).

3.3. Head mesoderm and ectoderm cell proliferation is heterogeneous in space and time along the dorsolateral neural crest cell migratory pathway

Considering the large expansion of the head tissue during the stages of neural crest migration (HH9-HH15, 24 h, Fig. 1A), we sought to understand the pattern of cell proliferation and tissue density changes, as well as cell-cell interactions with the neural crest. Previous studies have shown that the growth of the branchial arch is non-uniform over time (McLennan et al., 2012) but to determine the pattern of growth in space, we performed regional photoconversion of mesoderm and ectoderm *in vivo*. Transgenic quail (HH10) were mounted dorsal side down on EC culture (Chapman et al., 2001) for 405nm laser photoconversion of the Dendra2 photoconvertible protein (Fig. 3A and B). A region of interest was drawn roughly 100umx100umx50um and scanned with the 405nm laser until the DendraRed signal no longer increased. Embryos were re-incubated for an additional 6–8 h, imaged, and the dimensions of the photoconverted subregions were re-measured (Fig. 3C). We find that the photoconverted subregions in both mesoderm and ectoderm expanded in the mediolateral direction (along the dorsolateral neural crest migratory pathway and near the neural tube) but remained constant in the dorsal-ventral direction (Fig. 3D). In the anterior-posterior direction (along the vertebrate axis), the photoconverted subregions reduced in size for the mesoderm but remained constant for the ectoderm (Fig. 3D). Together, these data suggest that tissue growth within the paraxial mesoderm and overlying surface ectoderm expands the domain in the proximal-to-distal axis in the direction of neural crest migration more than in orthogonal directions.

To examine the pattern of tissue growth in cellular detail, we studied the distribution of BrdU-labeled mesoderm, ectoderm and neural crest cells between stages HH9 and HH15 to understand if proliferation is a contributor. Pulsed BrdU labeling was executed *in ovo* and we measured the number of BrdU positive cells from confocal z-stacks in optically-cleared chick embryos (Fig. 4A). The total number of embryos analyzed for each stage is 3 for HH9, 3 for HH11, 5 for HH13 and 5 for HH15. We segmented nuclei based on methyl green staining, then categorized the tissue as either ectoderm (by distance from the surface), migrating neural crest cells (using HNK-1), or mesoderm (Fig. 4B). A cell was categorized as BrdU positive and in S-phase if the intensity was above a threshold. We find that overall, between HH9 and HH15, there is substantial inhomogeneity in BrdU labeling in space and time (Fig 4A, F–H). For instance, at HH9, there are fewer cells in S-phase near the midline and the staining increases in frequency more laterally (Fig. 4A,G). By HH13-15 there are many subregions of high or low BrdU labeling. We next specifically examined the percentage of BrdU-positive mesodermal cells along the dorsolateral neural crest cell migratory pathway from r4 to ba2 in 50 μm bins starting at the midline to the end of the tissue (Fig. 4C–H). We found that the fraction of BrdU-positive mesodermal cells was highest in the subregion distal to the invasive neural crest cells within a range of approximately 100 μm in length, beginning prior to neural crest cell exit from the mid-r3 to mid-r4 neural tube and through to HH15 (Fig. 4G, dashed line).

At HH15, the BrdU pattern changes to be higher in the paraxial mesoderm near the dorsal neural tube midline and uniform throughout the remainder of tissue towards ba2. Similar measurements were performed on the tissue moving towards ba1 for comparison (Fig. 4C,F, Fig. S3). Along the neural crest cell migratory pathway towards ba1, the fraction of BrdU-positive cells was higher in the distal subregion at HH9, but this pattern becomes homogeneously distributed along the dorsolateral pathway from HH11-13 (Fig. S3). We measured a small increase in BrdU labeling in mesodermal cells in the paraxial mesoderm adjacent to rhombomere 1 (r1) at HH15 (Fig. S3). We also measured the fraction of BrdU-positive mesodermal cells in the region distal to r3 (Fig. 4D,F). Branchial arches 1 and 2 protrude outward from the embryo while this region does not extend as much. A smaller fraction of these cells are BrdU labeled between stages HH9-HH13 but the fraction increases at HH15 to be more similar to the proliferation in ba1. Similarly, we measured the BrdU labeling in the surface ectoderm overlying the path from near r4 to ba2 and found a higher percentage of cells were labeled with BrdU between stages HH9 and HH13 (Fig. 4F,H). In contrast to the mesoderm, the BrdU labeling was more or less constant throughout the region, with the exception of HH11, where there is a higher fraction of cells labeled towards the lateral edge of the tissue (Fig. 4H).

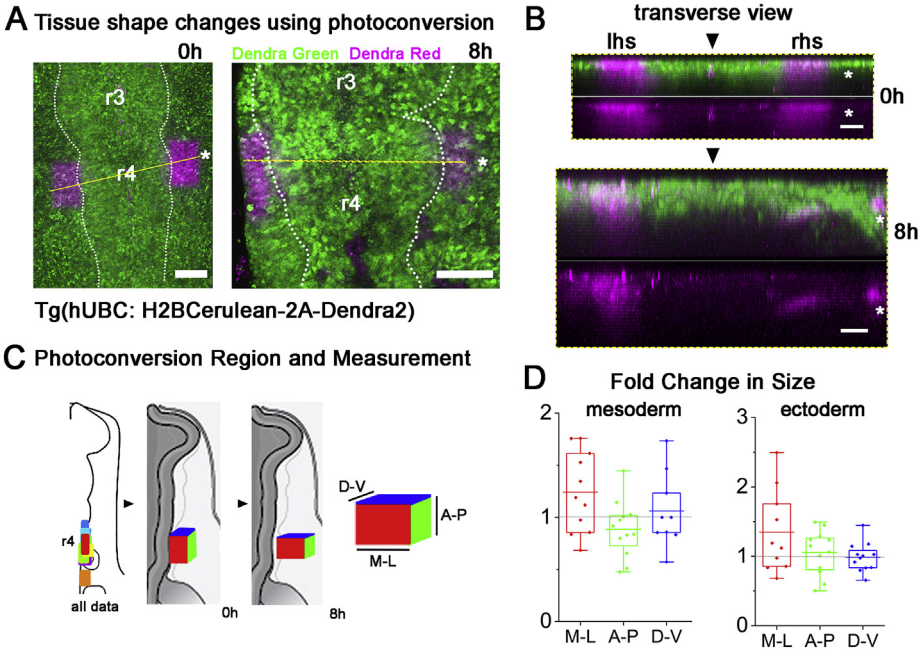

Fig. 3. Photoconverted region of tissue grows more in the dorsolateral than in the anterior-posterior direction. (A) Rectangular regions where Dendra2 was photoconverted from green to magenta in HH9 embryo and imaged again 8 h later. Scale bar 100um. (B) Transverse views through embryo in (A) at the dashed yellow line highlighting the depth of photoconversion. Scale bar 50um. (C) Schematic of embryos indicating locations of photoconverted regions at HH9. Also, schematic of embryo with box showing the growth of the tissue in the medial-lateral (M–L) direction and compression in the anterior-posterior (A–P) direction but no change in the dorsal-ventral (D–V) direction. Colors of the side of the box coordinate with colors in graph. (D) Fold change in size of mesoderm photoconverted region in each direction. No change marked with horizontal dashed line. n = 13 embryos.

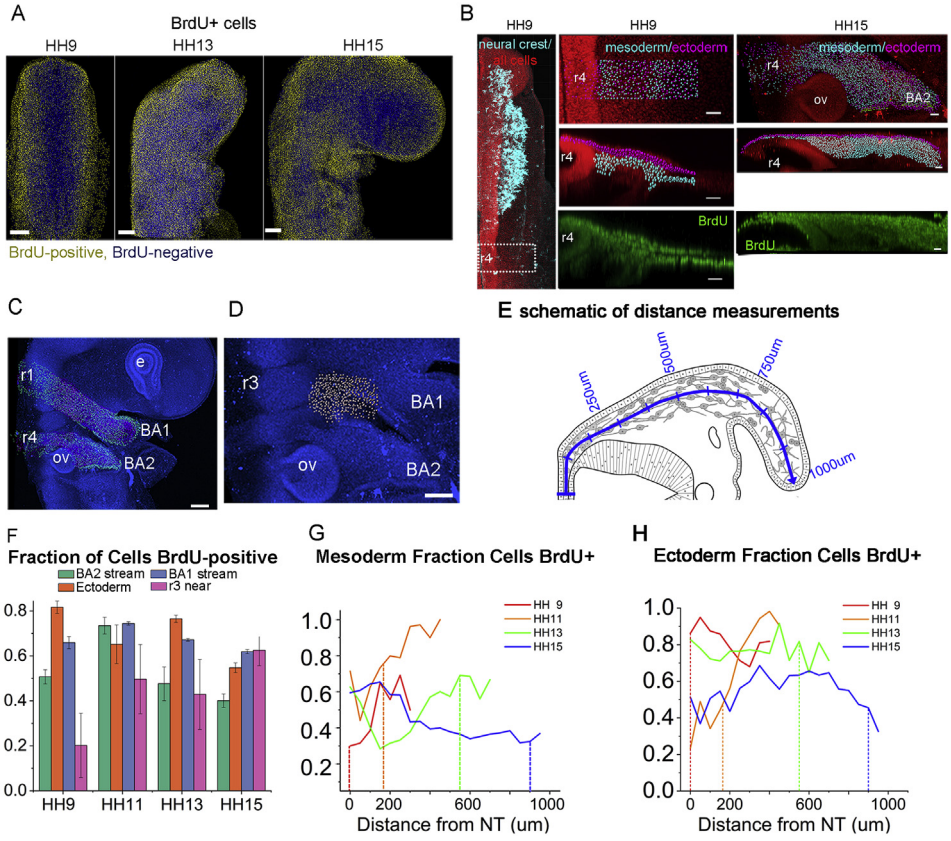

Fig. 4. BrdU labeling of cells changes over time and throughout the tissue. (A) Averaged images of embryos from HH9, HH13 and HH15 with yellow nuclei if the Brdu/methyl green intensity is in the top 40% of cells. Scale bar 100um. (B) HH9 embryo with nuclei (red), neural crest (cyan) and BrdU (green). Second column of images shows area in dashed rectangle with spots segmented on the methyl green channel indicating location in the mesoderm (cyan) or ectoderm (magenta). Third column, HH15 labeled similarly. Scale bar 40um. (C) HH15 embryo with ba1 and ba2 streams marked mesodermal cells (cyan) and ectoderm (magenta). Scale bar 100um. (D) Area lateral to r3 studied marked with white spots. Scale bar 100um. (E) Schematic of distance measurement from the neural tube curving along the neural crest pathway. (F) Fraction of mesodermal cells in ba1, ba2, ectoderm overlaying the ba2 stream, or cells adjacent to r3 domains that are positive for BrdU label in stages HH9-HH15 with SEM bars. (G) Fraction of mesodermal cells BrdU-positive in 50um bins along the domain of r4 to the end of ba2. Dashed vertical lines represent the front of the neural crest stream. (H) Fraction of ectoderm cells BrdU-positive in 50um bins along the domain of r4 to the end of ba2.

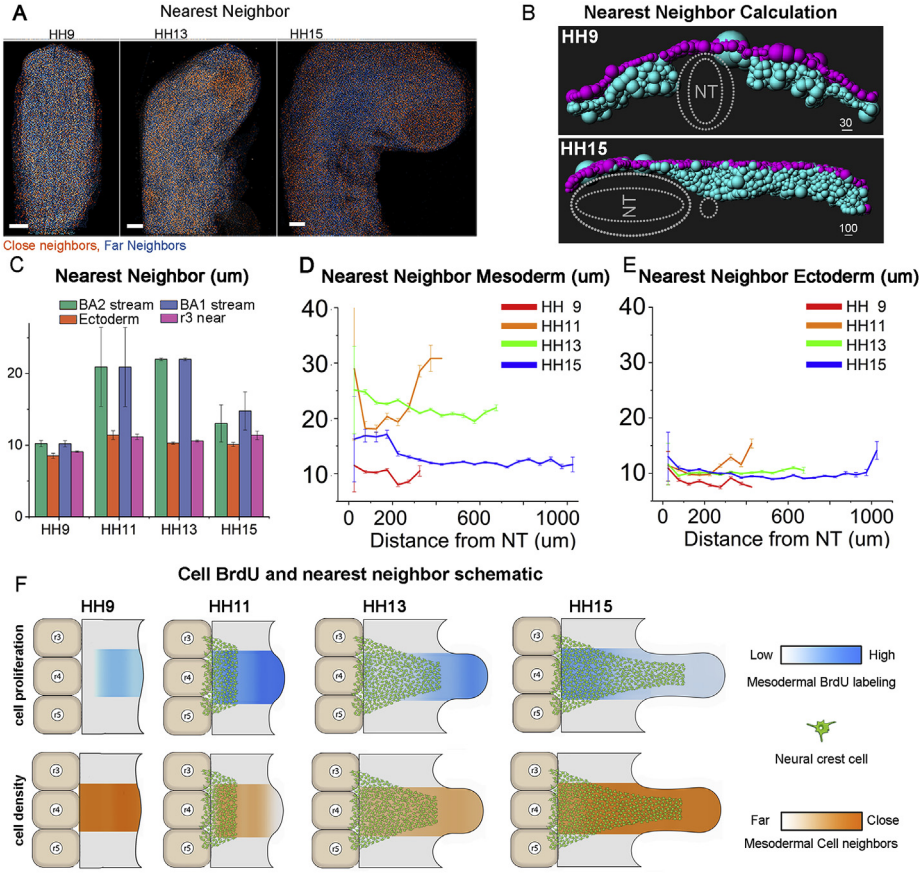

Fig. 5. Density of cells remains constant through out the r4 neural crest pathway. (A) Averaged images of embryos from HH9, HH13 and HH15 with orange nuclei indicating the densest 40% of cells. Scale bar 100um. (B) Transverse view of individual cells (mesoderm in cyan, ectoderm in magenta) in the r4 stream at HH9 (above) and HH15 (below) shown by spheres of sizes representing distance to their nearest neighbor. Larger spheres have distant neighbors, small spheres have a close neighbor. (C) Nearest neighbor distance averaged for all mesodermal cells for ba1 and ba2 streams, ectoderm overlaying the ba2 stream, and area lateral to r3 with SEM bars. (D) Nearest neighbor distance between mesoderm neighbors in 50um bins along the domain of r4 to the end of ba2. (E) Nearest neighbor distance between ectoderm neighbors. (F) Schematic of neural crest migration, tissue density (orange) and proliferation (blue) changes over time.

3.4. Cell density remains constant within proliferating mesoderm implying tissue growth expansion

To address whether cell proliferation of the head mesoderm translates into an increase in local cell density and/or an increase in tissue size, we measured the nearest neighbor distance between every detected cell nuclei within the mesoderm between HH9 and 15 (Fig. 5A and B). We find that the subregions of high BrdU label do not coincide with higher cell density (Fig. 5A, orange cells). The average distance to each cell's nearest neighbor was calculated for each stage (Fig. 5C) and in 50um subregions along the dorsolateral pathway (Fig. 5D and E). We attempted to also measure actual density within the tissue (Fig. S4) but due to the inaccuracies in measuring volume, we feel the nearest neighbor distance is more accurate. Using the nearest neighbor distance as a proxy for density, we find that the cell density is relatively constant through the subregion (Fig. 5D), with the exception of HH11. At HH9, mesodermal cells are tightly packed with an average of only 10 μm, or a typical cell nucleus length, between neighbors (Fig. 5C and D). As the tissue grows, mesodermal cells become less dense at HH11 and HH13 (24 μm and 21 μm between neighbors on average, respectively) but pack in more tightly again by HH15 (13 μm). The ectoderm is, in general, more packed with cells than the mesoderm and does not vary through stages or with spatial location (Fig. 5E). A schematic describing the neural crest stream development, proliferation and density can be found in Fig. 5F. These data support the concept that mesodermal cell proliferation gives rise to tissue growth since the areas of high BrdU labeling coincide with more loosely packed mesoderm.

3.5. Computer model simulations reveal a modest change in neural crest cell speed is required to respond to non-uniform domain growth

The non-uniform expansion and density variations of the mesoderm as determined above, plus the faster and more directed nature of the *in vivo* neural crest cells, creates a unique problem set for the collective migration of the neural crest. To explore the effects of non-uniform domain growth profiles on the neural crest cell migratory pattern, we exploited the strengths of our computer model (Fig. 6). We considered three distinct non-uniform domain growth profiles in which the domain growth was twice as fast within either the proximal or distal subregions of the domain (Fig. 6A). Specifically, we considered domain growth in the distal half of the domain (Fig. 6A; Distal (D)), the proximal half of the domain (Fig. 6A; Proximal (P)), and a combination of distal and proximal growth to mimic the empirically measured data presented in Fig. 4 (Fig. 6A; Mixed (M)). Each simulation was run for 24 hrs embryonic time and measurements were collected. In all simulations, the distribution of neural crest cells was measured at 24 hrs (Fig. 6B).

In the scenario of increased distal domain growth, the model predicts that the furthest distance traveled by cells is reduced in comparison with the uniform growth (Fig. 6A; compare U vs. D). In contrast, when the proximal subregion of the domain grows twice as fast compared to the distal subregion, the model predicts that cells travel further than with the uniform domain growth profile (Fig. 6A; compare U vs P). By combining the distal and proximal growth profiles to align with the empirical measurements where early there is more distal growth and at 18 hrs the growth switches to proximal (Fig. 4), we find the model predicts that there must be an increase in input neural crest cell speed in order for cells to reach the domain in 24 hrs (Fig. 6A; see mixed (M) with cell speed s = 48 μm/hr). The neural crest have two speed components: the input speed (Fig. 6) as well as an advection speed as they are carried by the domain growth. When input neural crest cell speed is increased, the stream length monotonically increases (Fig. 6B). This may be clarified by visualizing the changes in neural crest cell overall speed from the neural tube exit as a function of increasing cell speed from 42 μm/hr to 51 μm/hr (Fig. 6B). Note that if the neural crest cell speed is increased too high (51 μm/hr), the neural crest cells have to slow their speed during the last portion of migration so as not to over shoot the target (Fig. 6B). Together, the model simulations predict that neural crest cells must undergo a modest increase in cell speed from 42 to 48 μm/hr (approximately 14%) in order to reach the vicinity of the end of the migratory domain.

3.6. The pattern of cell proliferation and tissue growth of the head mesoderm is altered after ablation of premigratory neural crest cells

With our observed changes in mesodermal cell speed and directionality in culture in the presence of neural crest cells and heterogeneity of tissue growth in space and time, we sought to better understand the influence of migrating neural crest cells on this pattern. To address this, we ablated the dorsal one-third of the neural tube in a bilateral manner from mid-r3 to mid-r5 in HH9 embryos to significantly reduce the number of premigratory neural crest cells (Fig. 7A). After 24 hrs of egg re-incubation

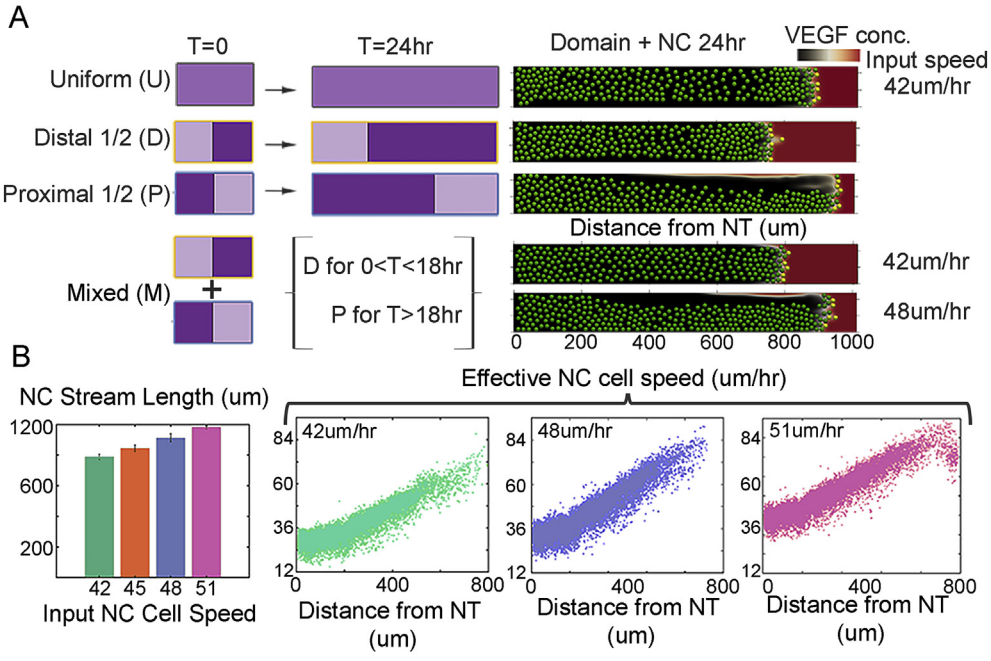

Fig. 6. Modeling simulations of non-uniform tissue growth and the neural crest cell migratory pattern. (A) Schematics of tissue growth profiles. Darker color indicates a higher growth rate. The growth rate is doubled for half of the domain in models D and P. As the cells migrate into the domain, they are advected at different rates and also actively migrate to reach the end of the domain. Right, example of final distribution of cells (green) on a domain with chemoattractant concentration (red/black color bar). Model M combines proximal (P) and distal (D) growth profiles such that for less than 18 h embryonic time the domain follows model D and from time greater than 18 h the model follows growth profile P, with input cell velocity of 42um/min. (B) Left: Length of the simulated neural crest cell migratory stream at 24hrs using different input cell speeds (42,45,48,51 μm/hr). Right: neural crest speed throughout the domain with different input speeds (42,48,51 μm/hr) as cells are also advected with the domain growth.

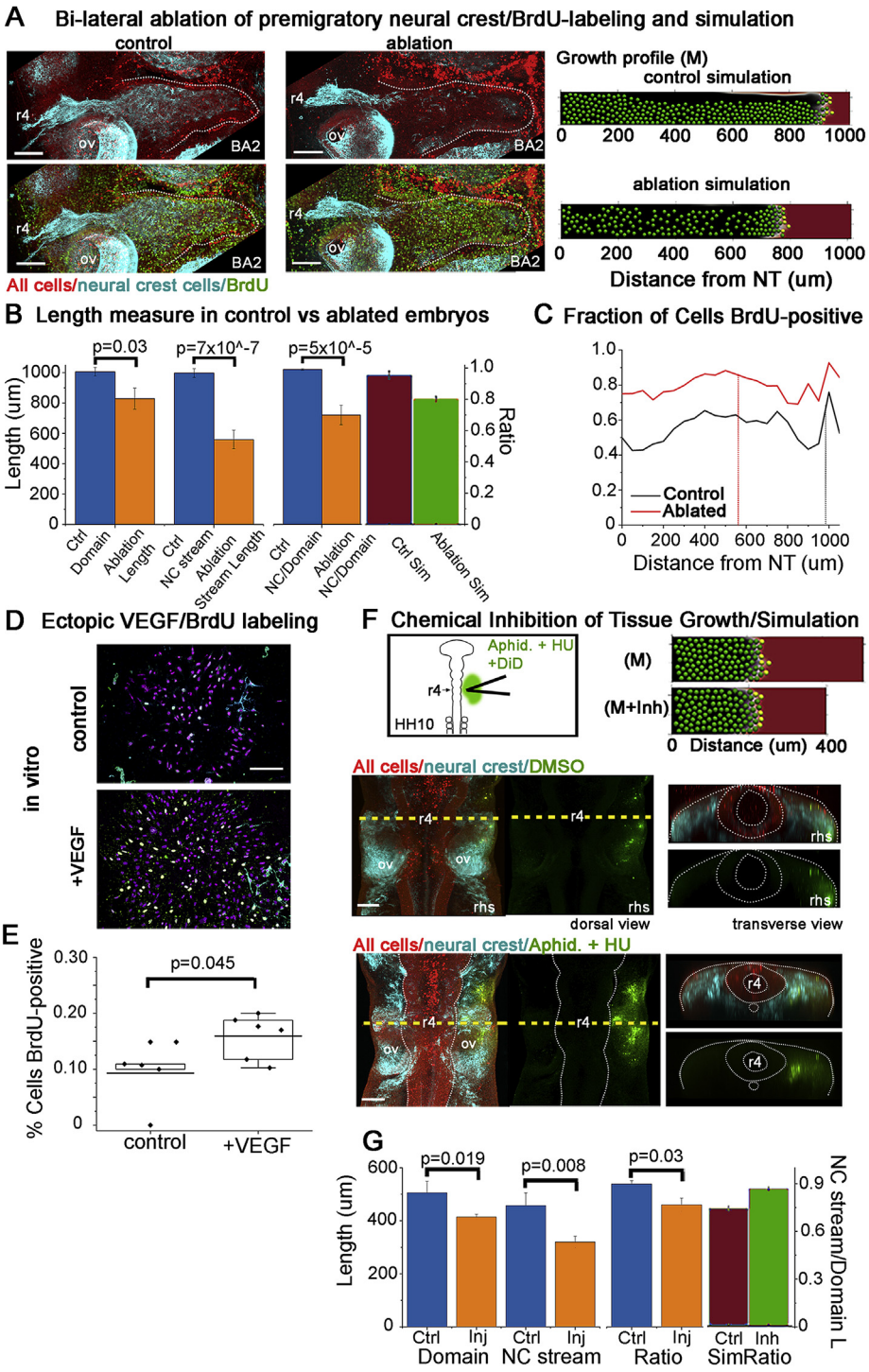

Fig. 7. Physical ablation of premigratory neural crest cells or chemical inhibition of mesoderm growth show effects on both the neural crest cell migratory pattern and tissue growth. Representative r4 neural crest cell migratory stream 24 hrs post bi-lateral ablation of premigratory neural crest cells: (A) Control (left) and ablated (right) stained with methyl green for all nuclei (red), HNK-1 for neural crest (cyan) and BrdU for proliferation (green). Scale bar 100um. The simulated control and ablation (modeled by reduction in number and delay of cells entering the domain) of premigratory neural crest cells (far right panels) scenarios with growth profile (M) as mentioned in Fig. 6. (B) Length of domain and neural crest stream and the ratio for control and ablated embryos, n = 10 for ablated and 12 for control. Far right bars (green/red) are the ratio of neural crest stream to domain length in simulated neural crest ablations. (C) Fraction of non-neural crest cells in domain BrdU positive for control and ablated embryos. Vertical line indicates average length of neural crest stream. (D) Schematic of VEGF IHC and the potential increase in VEGF concentration post neural crest ablation. Below, images of mesodermal cells in culture with or without exposure to VEGF for 16 h labeled with Hoescht for nuclei (magenta), HNK-1 for neural crest (cyan) and BrdU (green). Scale bar 100um. (E) Fraction of mesodermal cells *in vitro* that are BrdU-positive with (n = 5) or without VEGF (n = 8). (F) Schematic and representative embryo injected with a cocktail of aphidicolin, hydroxyurea and DiD (green) after 8 h incubation. IHC performed with methyl green (red) and HNK-1 (cyan). Scale bar is 100um. The simulated control and domain growth inhibition panels are shown on the far right after 8 h of simulation time to correspond to the experimental data. (G) Length of domain and neural crest stream and ratio of 8 treated and 8 control embryos. Far right bars (red/green) are the ratio of neural crest stream length to domain length in simulated chemical inhibition of domain growth.

to HH15, BrdU labeling was applied *in ovo* before embryos were harvested, fixed and processed for immunolabeling of the migrating neural crest cells with HNK-1. In silico, we ran simulations of the ablation of premigratory neural crest by reducing the number of migrating cells (to accurately capture some cells that escape ablation in the experiment) and delaying entry into the domain, using the mixed (M) growth profile above (Fig. 7A, right). We measured the distal length from the neural tube midline to the brachial arches along the presumptive dorsolateral neural crest cell migratory pathway, and found this distance was significantly reduced in ablated embryos in comparison to controls (Fig. 7B). Simulations showed that the ratio of the migratory domain length to neural crest cell stream front was also reduced (Fig. 7B; red/green bars). Examination of the pattern of BrdU-labeled mesodermal cells revealed that cell proliferation was higher along the length of the domain at every position and, at the distal-most locations, increased by 24% (Fig. 7A,C).

It has been shown that the surface ectoderm expresses VEGF which is a proliferative inducing agent as well as a chemoattractant for the neural crest (McLennan et al., 2010). Without the neural crest population binding to the VEGF expressed by the ectoderm, we examined the effects of increased VEGF on the mesoderm population by exposing mesoderm in culture to 100ug/mL VEGF. We found a significant increase in the percentage of dividing mesodermal cells (Fig. 7D and E). Thus, in the absence of migrating neural crest as in ablated embryos, increased proliferation of the mesoderm could be stimulated by increased exposure to VEGF.

3.7. Inhibition of mesodermal cell proliferation reduced domain size and length of the neural crest cell migratory stream

The computer model simulations presented above predicted significant changes in the neural crest cell migratory distance depending on the domain growth profile (Fig. 6A). To attempt a change in growth rate *in vivo*, we microinjected a cocktail of Aphidicolin (1 mg/mL), Hydroxyurea (5mM) and DiD into the most lateral mesoderm that could be reached in HH10 embryos (Fig. 7F). Aphidicolin and hydroxyurea are both well-known to inhibit the cell cycle in S-phase and halt proliferation (Levenson and Hamlin, 1993; Mutomba and Wang, 1996). We microinjected control embryos with 10% DMSO and DiD. All microinjected embryos were re-incubated for 8 hrs then labeled with HNK1 to fluorescently label migrating neural crest and methyl green to mark all cells (Fig. 7F). While we anticipate the chemicals to spread further than the DiD marked area, we also anticipate that in only 8 hrs of re-incubation, the subregions with higher fractions of S-phase cells marked with BrdU (from Fig. 4G and H) will be most highly affected. That is, the most lateral parts of the mesodermal domain will be halted in S-phase. In silico, we modeled the inhibition by reducing domain growth throughout the two-dimensional space (Fig. 7F). We find that both the mesoderm within the dorsolateral domain and neural crest cell migratory stream were shorter in experimentally treated embryos (Fig. 7G). The ratio of the length of the neural crest cell migratory stream to the total length of the branchial arch tissue was significantly reduced (Fig. 7G). In contrast, in simulation of inhibited domain growth, the ratio of the neural crest cell migratory stream to the domain length increased in the presence of an inhibitor (Fig. 7G; red/-green bars). This could be explained in that our model does not include a feedback mechanism between the neural crest and mesoderm so the neural crest cells are able to continue their migratory program unphased by the size or growth rate of the domain and travel further into the stream. Thus, by chemically inhibiting cell proliferation in the mesoderm (and probably ectoderm), we were able to reduce tissue growth but, more importantly, alter the resulting neural crest stream length.

3.8. In vivo time-lapse imaging reveals distinct collective motions of head mesoderm and ectoderm cell behaviors prior to neural crest emergence

The *in vivo* time-lapse measurements of neural crest and mesoderm interactions, speed and directionality beg the analysis of the mesoderm before the neural crest emerge near r4. When embryos were imaged prior to neural crest emergence, we observed a few interesting phenomena

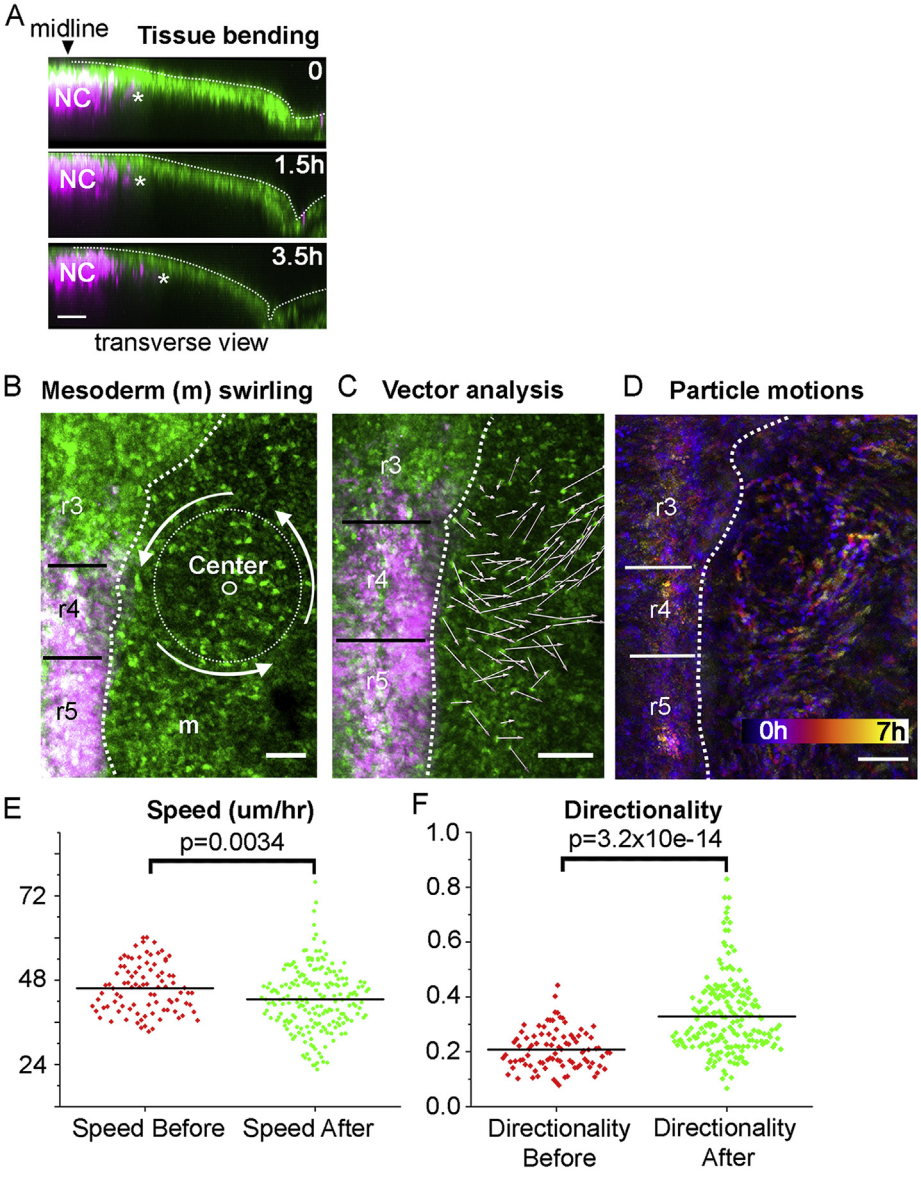

Fig. 8. *In vivo* time-lapse imaging of head mesodermal cell behaviors pre neural crest emergence. (A) Transverse view of r4 area over 3.5 hrs in a time-lapse. Neural crest (magenta, leader marked with star) have just emerged from the neural tube while the surface ectoderm is changing shape. Scale bar 50um. (B) Image of embryo at beginning of time-lapse with center of whirling motion and approximate size of circle marked. Scale bar 100um. (C) Displacement of mesodermal and ectoderm cells (white arrows) over 8 hrs of imaging. (D) Color-coded time projected over a 2 hr window with purple being time zero and yellow 2 hrs later. The circular rotation of cells can be seen across from the r3/r4 boundary. Comparison of Speed (E) and Directionality (F) of mesodermal cells before and after the neural crest emerge from r4.

(Fig. 8). First, as neural crest cells are emerging from the neural tube and beginning to migrate, the ectoderm can be seen to bend and change shape as the embryo grows (Fig. 8A and Movie 9). The large morphological changes to the embryo alter the presumptive path of the neural crest, from at first being relatively straight, to a curved path following the ectoderm deflection. Second, mesoderm and ectoderm cells adjacent to the dorsal hindbrain moved in a counter-clockwise whirling pattern prior to the emergence of neural crest cells (Fig. 8B–D, Movie 7). The whirling pattern of cells was observed in 7 of 12 embryos when the time-lapse was begun before the 10 somite stage. The whirling pattern had a diameter of approximately 125 μm and was centered adjacent to r3. Mesoderm and ectoderm cells rotated together at 0.2° per minute, suggesting that one revolution would take approximately 30 hrs to complete and cannot be fully visualized here. The whirling cells were at least 50 μm deep into the tissue but the maximum depth could not be determined due to the lack of light penetration into the tissue. Interestingly, the whirling behaviors of the mesoderm and ectoderm stopped coincident with the emergence of the r4 neural crest cells (Movie 7). Further, the pattern of mesodermal cell behaviors on the left-hand side of the embryo rotated in a clockwise manner (data not shown). The whirling effect was not observed in other locations or at later time points. Cell tracking and analysis showed that mesodermal cells 'before' neural crest emergence moved at 46 μm/hr on average with directionality of 0.21 which is slower and less directed than 'after' neural crest cells emerged (Fig. 8E and F).

Supplementary video related to this article can be found at https://doi.org/10.1016/j.ydbio.2020.02.010.

4. Discussion

Previous static studies have suggested that head mesoderm (through which neural crest cells travel) grows in a uniform manner in space (McLennan et al., 2012) and neural crest cells are passively carried along (Noden and Trainor, 2005; Evans and Noden, 2006) rather than actively migrating. Our discovery of the inherent motility of individual mesodermal cells in culture, and dramatic changes in cell behaviors in the presence of cranial neural crest cells, suggest a more complex and dynamic choreography of vertebrate head morphogenesis. *In vivo* imaging and experiments demonstrated the rich spatio-temporal pattern of ectoderm and mesodermal cell dynamics, and cell-cell interactions with migrating neural crest cells. Mathematical model simulations of variable domain growth profiles confirmed the robustness of cranial neural crest migration in the complex environment of the growing domain. Overall, we present a descriptive analysis showing neural crest and mesoderm can behave as independent migratory populations but are influenced by the presence and behavior of each other.

Head mesodermal cells in culture displayed inherent dynamic migratory behaviors *in vitro*, suggesting these cells are capable of active cell movements *in vivo* and could exchange neighbor relationships. Mesodermal cells isolated from the chick head paraxial mesoderm adjacent to the rostral hindbrain dispersed as individuals throughout the culture dish in a similar manner to neural crest cells that exit cultured neural tube explants (Fig. 1). Mesodermal cells in culture moved 81% slower but 155% more directed than neural crest cells *in vitro* (Fig. 1). This was surprising since paraxial and lateral mesoderm have previously been assumed as passive tissue (Noden and Trainor, 2005; Evans and Noden, 2006). Interestingly, when placed in co-culture with neural crest cells, both mesodermal and neural crest cells migrated faster and freely intermingled (Fig. 1). Thus, the inherent motility of head mesodermal cells and dynamic interplay with the neural crest and ectoderm in culture, mean that cell behaviors must be closely coordinated *in vivo* to create the stereotypical pattern of the head and branchial arches.

In the embryo, mesodermal cells displayed directed mediolateral motion and interacted with invading neural crest cells, suggesting a close coordination between the neural crest and mesodermal cells to expand tissue growth and morphogenesis of the branchial arches. Unlike *in vitro*, the mesodermal cells moved as a collective, keeping spatial order. Both cell types moved more slowly *in vivo*, most likely due to the presence of extracellular matrix components, other cell types and three-dimensional spatial restrictions. As *in vitro*, mesodermal cells that interacted with neural crest cells displayed more directed cell trajectories (Figs. 1 and 2G, circles) however, instead of mixing, some mesodermal cells were displaced either lateral or off the migratory pathway after interacting with a neural crest cell (Fig. 2G, triangle). The fact that neural crest and mesodermal cells interacted was not surprising given previous data from quail-chick chimeras or viral labeling studies that reported populations of these two cell types developed in close registration (summarized in Le Douarin and Kalcheim, 1999; reviewed in Noden and Trainor, 2005). However, it was stunning to observe the rich individual mesodermal and neural crest cell-cell interactions and rapid movements of neural crest cells to overtake individual mesodermal cells en route to the branchial arches (see Movie 6). We did not observe neural crest cells to be solely carried along passively by the underlying moving mesoderm tissue (Evans and Noden, 2006), but this may occur later during branchial arch patterning. Intriguingly, neural crest cells that were observed to displace loosely-connected mesodermal cells would require cell contact with enough force to change the direction of the contacted cell. Further time-lapse studies that focus on local mesodermal and neural crest cell-cell interactions combined with an examination of the expression of cell receptor-ligand pairs should help to better understand the dynamic relationship between these two cell types and the transition of the mesodermal cells to lateral movement.

Mesoderm tissue growth is non-uniform in space and differs from the ectoderm, suggesting more complex cell dynamics than previously thought. Photoconversion of small volumes of paraxial mesoderm tissue (Fig. 3) showed the tissue is expanding in the lateral direction more than in any other direction. BrdU-positive cell numbers increased laterally through the mesoderm domain between HH9 and HH13, hinting that there was higher cell proliferation towards the lateral end of the domain; the density of the cells remained constant (Fig. 4; with the exception of HH11). In addition, our time-lapse movies show a flow of mesodermal cells towards the lateral end of the domain without major cell rearrangements, leapfrogging or circulation (Fig. 2A) implying tissue expansion is driven by proliferation and lateral movement of the mesoderm. The ectoderm overlying the mesoderm domain had an even higher fraction of cells positive for BrdU, but in general is a more densely packed tissue such that every division may not result in expansion. We conclude that the mesoderm is therefore the main driver of growth in the lateral direction pushing the branchial arch formation. Comparing the area adjacent to r3, where there is less expansion, a smaller fraction of mesodermal cells are positive for BrdU and the tissue is denser until stage 15 when the arches are poised to fuse together and perhaps another pattern of growth could be taking shape.

Despite the non-uniformity in tissue growth in space and time, migrating neural crest cells remained as a continuous stream of cells. Our data indicated that during neural crest migration to the branchial aches (HH11-15) the mesoderm is proliferating ahead of the neural crest migratory front (Figs. 4G and 5F; highest fraction of BrdU positive cells beyond the neural crest stream). Neural crest cells must then actively migrate to stay in pace with the branchial arches (Fig. 5F). In analogy, the neural crest cells are on a moving walkway in which the different sections of the walkway move faster/slower over time. How the neural crest cells modulate advection and active migration while traveling through the mesoderm will be exciting to examine mechanistically in the future.

Computational modeling allowed us to rapidly compare the effect of non-uniform domain growth on the neural crest stream pattern and test the hypothesis that cells must change speed to compensate. When we tested either enhanced growth of the distal-half (D) or proximal-half (P) of the domain, we learned that the stream length was longer with proximal growth since the neural crest cells were able to be advected by the domain for longer periods of time. However, distal growth of the domain more accurately captured our empirical data (for the first 18 hrs of neural crest migration) and the resulting shortened neural crest stream

suggested cells must increase speed to compensate (Fig. 6A). By combining the empirically measured proximal domain growth into the simulation for the last portion of the process (from 18 to 24 h), this promoted the follower cells to maintain the collective stream migration (Fig. 6A). When we tested the change in cell speed to compensate for domain growth, we found that an increase from 42 to 48 μm/hr (approximately 14%) was adequate for the stream to reach nearly the end of the domain in 24 hrs (Fig. 6B). Together, this suggests that neural crest cell migration is a combination of advection and active migration with only a modest increase in cell speed required for the neural crest to compensate for non-uniform tissue growth over a 24hr period of migration.

The pattern of BrdU staining and tissue growth of the head mesoderm was altered after ablation of premigratory neural crest cells, suggesting VEGF (or other growth factor signals) promotes both neural crest migration and mesoderm proliferation simultaneously. After ablation of premigratory r4 neural crest cells, ba2 formed but was smaller than in control embryos (Fig. 7A,C) agreeing with previously published observations that branchial arch tissue can form independent of the neural crest cells (Veitch et al., 1999). A large fraction of the tissue in the branchial arches is composed of neural crest cells (Fig. 1A) so to make up the volume lost after the ablation, we reasoned that the mesoderm must increase in its proliferation (Fig. 7C). When we simulated the ablation of premigratory neural crest cells, we learned that the domain length was unaffected and cells that escaped ablation did not reach the end of the normal growing domain since the model does not have a feedback mechanism between the mesoderm and neural crest (Fig. 7A and B). We suggest that VEGF may have a dual role to play by acting as a chemoattract for the neural crest (McLennan and Kulesa, 2010; McLennan et al., 2010) and as a proliferative agent. We found that cultured mesodermal cells overproliferated in response to VEGF added to the media (Fig. 7D and E). These data support previous observations that branchial arch tissue can form independent of the neural crest cells and suggest the increase in proliferation of mesodermal cells may result from an overabundance of VEGF. However, the downstream morphogenesis of muscle and bone would still be affected (Noden, 1988; Veitch et al., 1999). It is possible that there are other signals or growth factors originating in the dorsal neural tube that could influence either the proliferation or cell motion of the mesoderm that were ablated with the neural crest, however the presence of VEGF has already been established and seems a likely candidate (McLennan et al., 2010). If the VEGF, or other factor, induces the growth of the mesoderm at r4, then it might stand to reason that the same factor could be acting adjacent to r3 where there are no neural crest cells but there are fewer proliferating cells in this region (Fig. 4F). However, a BMP inhibitor, DAN (NBL1), was found in the area adjacent to r3 and inhibits proliferation in neural crest (McLennan et al., 2017). It is possible that there are other mechanisms at work in the area adjacent to r3 to repress the growth of the cleft between the arches.

We also asked the converse question, if the branchial arches were to diminish in size, what effect would this have on the migratory neural crest stream? Chemical inhibition of cell proliferation in the mesoderm led to reduced length of ba2, but the neural crest cell migratory stream length was also significantly reduced (Fig. 7F and G). We expected the neural crest cells to travel further into the branchial arch with a shorter domain following their own program for invasion and proliferation in the branchial arches. However, since the neural crest cells traveled a shorter distance through the migratory domain (Fig. 7F and G), this implied a signaling interplay between the independent motion of the neural crest and growth activity of the mesoderm or ectoderm. Future model simulations that test hypothetical feedback mechanisms between the neural crest and mesoderm to either stimulate or inhibit growth and migration will help to shed light on this question.

Another interesting result of our time lapse studies was the behavior of the ectoderm and mesodermal cells prior to neural crest migration. The cells displayed large scale collective whirling motions lateral to r3 (prior to neural crest cell emergence). Whirling patterns of cells have been observed in many contexts, from confluent fibroblast cultures (Elsdale and Wasoff, 1976) to vertebrate gastrulation in the tailbud of zebrafish and chick embryos, especially within the mesodermal progenitor zone (MPZ) (Zamir et al., 2006; Lawton et al., 2013; Mongera et al., 2018). Curiously, the observance of a large scale, circular structure has previously been reported in chick head mesoderm and visualized using stereo scanning electron microscopy (Meier, 1981; Jacobson, 1988). It was observed that paired mesodermal cell disks, which were termed 'somitomeres,' with a diameter ranging from 135 to 240 μm, appear in an anterior-to-posterior order starting at about HH4 through HH9. Cells were arranged around one or two central cells with a tuft of processes pointing toward the ectoderm (Meier, 1981; Jacobson, 1988). When we measured ectoderm and mesodermal cell movements within presumed somitomeres, we found that cells traveled in a counter-clockwise direction on the right-hand-side of the embryo (and clockwise on left-hand-side) at a speed of 0.2° per minute (Fig. 8B–D). Further analysis of mesodermal cell-cell interactions and changes in tissue boundary geometries or molecular signals in the microenvironment in the vertebrate head should help us better understand the functional relationship between whirling motions, tissue growth, and the emergence of the migrating neural crest cells.

In conclusion, our results support a model wherein neural crest cells balance active motility and growth-driven advection to preserve movement as a collective cell population. Paraxial mesodermal cells are inherently motile and display collective cell movements that transition from large-scale whirling (prior to neural crest cell emergence) to directed trajectories towards the branchial arches. By simultaneously observing ectoderm, mesoderm and neural crest cell behaviors, we have unraveled the complex cell dynamics that lead to head and branchial arch morphogenesis. Empirical measurements revealed spatiotemporal changes in tissue growth expansion that begin within the paraxial mesoderm and transition to the distal subregion of the forming branchial arches over time. By simulating neural crest cell migration in response to the experimentally measured tissue growth profile, we arrived at a better understanding of compensatory changes in neural crest cell speed. Our manipulation of the neural crest cell migratory domain by ablation of the premigratory neural crest or inhibition of mesodermal cell proliferation strengthen the idea that interactions between the two cell populations stimulate tissue growth. Lastly, our detailed analysis of avian head morphogenesis and neural crest cell migration now provide a framework to integrate single cell genomic data and comparisons between different vertebrate research organisms.

Funding

This work was supported by the kind funding of The Stowers Institute for Medical Research. R.E.B. is a Royal Society Wolfson Research Merit Award holder. H.G.O. is supported by National Institutes of Health award RO1GM029123. R.G. gratefully acknowledges funding from the Engineering and Physical Sciences Research Council (EP/G03706X/1).

Data availability

Original data underlying this manuscript can be accessed from the Stowers Original Data Repository at https://www.stowers.org/research/publications/odr.

Declaration of competing interest

No competing interests declared.

Acknowledgements

PMK would like to acknowledge the kind and generous funding from the Stowers Institute for Medical Research. We would also like to thank David Huss, Rusty Lansford, and the Translational Imaging Center at the

University of Southern California for use of the transgenic quail. In addition, we thank Dave Lei and Ashley Young for contributions to imaging and image analysis as part of the Stowers Summer Scholars Program.

Appendix A. Supplementary data

Supplementary data to this article can be found online at https://doi.org/10.1016/j.ydbio.2020.02.010.

References

Chapman, S.C., Collignon, J., Schoenwolf, G.C., Lumsden, A., 2001. Improved method for chick whole-embryo culture using a filter paper carrier. Dev. Dynam. 220 (3), 284–289. https://doi.org/10.1002/1097-0177(20010301)220:3.

Elsdale, T., Wasoff, F., 1976. Fibroblast cultures and dermatoglyphics: the topology of two planar patterns. Wilehm Roux Arch Dev Biol 180 (2), 121–147. https://doi.org/10.1007/BF00848102.

Evans, D.J., Noden, D.M., 2006. Spatial relations between avian craniofacial neural crest and paraxial mesoderm cells. Dev. Dynam. 235 (5), 1310–1325. https://doi.org/10.1002/dvdy.20663.

Hacker, A., Guthrie, S., 1998. A distinct developmental programme for the cranial paraxial mesoderm in the chick embryo. Development 125 (17), 3461–3472.

Hamburger, V., Hamilton, H., 1951. A series of normal stages in the development of the chick embryo. J. Morphol. 88 (1), 49–92. https://doi.org/10.1002/jmor.1050880104.

Hou, B., Zhang, D., Zhao, S., Wei, M., Yang, Z., Wang, S., Wang, J., Zhang, X., Liu, B., Fan, L., et al., 2015. Scalable and DiI-compatible optical clearance of the mammalian brain. Front. Neuroanat. 9, 19. https://doi.org/10.3389/fnana.2015.00019.

Huss, D., Lansford, R., 2017. Fluorescent quail: a transgenic model system for the dynamic study of avian development. Methods Mol. Biol. 1650, 125–147. https://doi.org/10.1007/978-1-4939-7216-6_8.

Jacobson, A.G., 1988. Somitomeres: mesodermal segments of vertebrate embryos. Development 104 (Suppl. l), 209–220.

Kontges, G., Lumsden, A., 1996. Rhombencephalic neural crest segmentation is preserved throughout craniofacial ontogeny. Development 122 (10), 3229–3242.

Kulesa, P.M., McLennan, R., 2015. Neural crest migration: trailblazing ahead. F1000Prime Rep 7. https://doi.org/10.12703/P7-02, 02.

Kulesa, P.M., Teddy, J.M., Stark, D.A., Smith, S.E., McLennan, R., 2008. Neural crest invasion is a spatially-ordered progression into the head with higher cell proliferation at the migratory front as revealed by the photoactivatable protein. KikGR', *Dev Biol* 316 (2), 275–287. https://doi.org/10.1016/j.ydbio.2008.01.029. TS0012-1606(08)00064-X [pii].

Lawton, A.K., Nandi, A., Stulberg, M.J., Dray, N., Sneddon, M.W., Pontius, W., Emonet, T., Holley, S.A., 2013. Regulated tissue fluidity steers zebrafish body elongation. Development 140 (3), 573–582. https://doi.org/10.1242/dev.090381.

Le Douarin, N., Kalcheim, C., 1999. The Neural Crest. Cambridge University Press, Cambridge, UK ; New York, NY, USA.

Levenson, V., Hamlin, J.L., 1993. A general protocol for evaluating the specific effects of DNA replication inhibitors'. Nucleic Acids Res. 21 (17), 3997–4004.

McKinney, M.C., McLennan, R., Kulesa, P.M., 2016. Angiopoietin 2 signaling plays a critical role in neural crest cell migration. BMC Biol. 14 (1), 111. https://doi.org/10.1186/s12915-016-0323-9.

McLennan, R., Bailey, C.M., Schumacher, L.J., Teddy, J.M., Morrison, J.A., Kasemeier-Kulesa, J.C., Wolfe, L.A., Gogol, M.M., Baker, R.E., Maini, P.K., et al., 2017. DAN (NBL1) promotes collective neural crest migration by restraining uncontrolled invasion. J. Cell Biol. 216 (10), 3339–3354. https://doi.org/10.1083/jcb.201612169.

McLennan, R., Dyson, L., Prather, K.W., Morrison, J.A., Baker, R.E., Maini, P.K., Kulesa, P.M., 2012. Multiscale mechanisms of cell migration during development: theory and experiment. Development 139 (16), 2935–2944. https://doi.org/10.1242/dev.081471.

McLennan, R., Kulesa, P., 2010. Neuropilin-1 interacts with the second branchial arch microenvironment to mediate chick neural crest cell dynamics. Dev. Dynam. : Off. Publ. Am. Assoc. Anat. 239 (6), 1664–1673. https://doi.org/10.1002/dvdy.22303.

McLennan, R., Teddy, J.M., Kasemeier-Kulesa, J.C., Romine, M.H., Kulesa, P.M., 2010. Vascular endothelial growth factor (VEGF) regulates cranial neural crest migration in vivo. Dev. Biol. 339 (1), 114–125. https://doi.org/10.1016/j.ydbio.2009.12.022.

Meier, S., 1981. Development of the chick embryo mesoblast: morphogenesis of the prechordal plate and cranial segments. Dev. Biol. 83 (1), 49–61.

Mongera, A., Rowghanian, P., Gustafson, H.J., Shelton, E., Kealhofer, D.A., Carn, E.K., Serwane, F., Lucio, A.A., Giammona, J., Campas, O., 2018. A fluid-to-solid jamming transition underlies vertebrate body axis elongation. Nature 561 (7723), 401–405. https://doi.org/10.1038/s41586-018-0479-2.

Mutomba, M.C., Wang, C.C., 1996. Effects of aphidicolin and hydroxyurea on the cell cycle and differentiation of Trypanosoma brucei bloodstream forms. Mol. Biochem. Parasitol. 80 (1), 89–102.

Noden, D., 1988. Interactions and Fates of Avian Craniofacial Mesenchyme. Development, Cambridge, England, pp. 121–140, 103 Suppl.

Noden, D., Trainor, P., 2005. Relations and interactions between cranial mesoderm and neural crest populations. J. Anat. 207 (5), 575–601. https://doi.org/10.1111/j.1469-7580.2005.00473.x.

Preibisch, S., Saalfeld, S., Schindelin, J., Tomancak, P., 2010. Software for bead-based registration of selective plane illumination microscopy data. Nat. Methods 7 (6), 418–419. https://doi.org/10.1038/nmeth0610-418. Tnmeth0610-418 [pii].

Preibisch, S., Saalfeld, S., Tomancak, P., 2009. Globally optimal stitching of tiled 3D microscopic image acquisitions. Bioinformatics 25 (11), 1463–1465. https://doi.org/10.1093/bioinformatics/btp184.

Prieto, D., Aparicio, G., Machado, M., Zolessi, F.R., 2015. Application of the DNA-specific stain methyl green in the fluorescent labeling of embryos. J Vis Exp 99, e52769. https://doi.org/10.3791/52769.

Schindelin, J., Arganda-Carreras, I., Frise, E., Kaynig, V., Longair, M., Pietzsch, T., Preibisch, S., Rueden, C., Saalfeld, S., Schmid, B., et al., 2012. Fiji: an open-source platform for biological-image analysis. Nat. Methods 9 (7), 676–682. https://doi.org/10.1038/nmeth.2019.

Szabo, A., Mayor, R., 2016. Modelling collective cell migration of neural crest. Curr. Opin. Cell Biol. 42, 22–28. https://doi.org/10.1016/j.ceb.2016.03.023.

Tosney, K.W., 1982. The segregation and early migration of cranial neural crest cells in the avian embryo. Dev. Biol. 89 (1), 13–24.

Veitch, E., Begbie, J., Schilling, T.F., Smith, M.M., Graham, A., 1999. Pharyngeal arch patterning in the absence of neural crest. Curr. Biol. 9 (24), 1481–1484.

Zamir, E.A., Czirok, A., Cui, C., Little, C.D., Rongish, B.J., 2006. Mesodermal cell displacements during avian gastrulation are due to both individual cell-autonomous and convective tissue movements. Proc. Natl. Acad. Sci. U. S. A. 103 (52), 19806–19811. https://doi.org/10.1073/pnas.0606100103.